ACS APPLIED ELECTRONIC MATERIALS

pubs.acs.org/acsaelm Article

Surface Dynamics of Charge Transport in $LaAlO_3/SrTiO_3$ with Time-Resolved Kelvin Probe Force Microscopy

Hugh Smith,* Liam Collins, and Alp Sehirlioglu

Cite This: ACS Appl. Electron. Mater. 2022, 4, 206−216 Read Online

ACCESS | Metrics & More | Article Recommendations | Supporting Information

ABSTRACT: Time-resolved Kelvin probe force microscopy (tr-KPFM) was used to map surface potential dynamics in LAO/STO under its critical thickness, where it acts as an insulator, as polarizing and depolarizing electric fields were applied to planar electrodes in ambient conditions. Two time constants, for polarization and relaxation (i.e., depolarization) each, were derived and were shown to be independent of the direction of electrical field, revealing the reproducibility and recovery of the surfaces. Ambient aging or recent electrical history did not change the surface kinetics as determined by tr-KPFM. During polarization, the faster time constant (∼3−6 s) is likely associated with the transport of H^+ ions through the full length of the channel. The slower time constant (∼40−50 s), on the other hand, is observed across only half the channel width near the higher-potential—more positive—electrode, which is likely associated with an electrochemical reaction such as the dissociation of water. This slower time constant drops to ∼10−20 s toward the middle of the channel which could represent the transport of OH^- ions. During relaxation, the fast time constant is consistent with polarization and is correlated to the same mechanism while the slower time constant is higher than it was during polarization and may represent the reabsorption of moisture from the atmosphere.

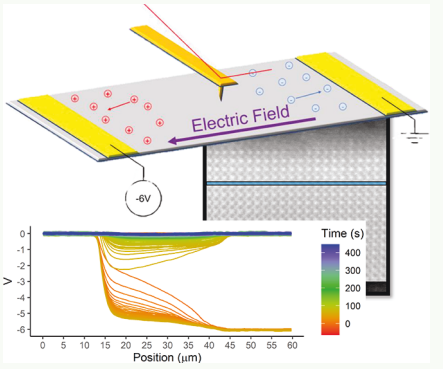

KEYWORDS: *tr-KPFM, heterostructures, surface kinetics, adsorbed species, time constants*

INTRODUCTION

Since its discovery, $LaAlO_3/SrTiO_3$ heterointerfaces have sparked tremendous interest both for a fundamental understanding of the unique observations, such as the tunable conductivity, magnetism, and superconductivity at low temperatures, and for its potential applicability as a high density, extreme environment transistor.[1−4] Fundamentally, in relationship to interface conductivity, the observations that needed elucidation were (i) the origin of charges, (ii) the presence of a critical thickness of the film above which the interface shows conductivity, (iii) buildup of dielectric potential across the film thickness, and (iv) the mechanism of tunability under an external field across the thickness of the film. Investigations revealed a complicated system that requires incorporation of many factors including stoichiometry of the films and the presence of antisites, oxygen vacancies in the substrate as well as in the film (specifically on the surface of the film), strontium vacancies in the substrate, intermixing, interfacial strain, and changes in the equilibrium positions of the atoms.[5−24] More recently, there has been significant research demonstrating that the surface defects (i.e., oxygen vacancies) and surface-adsorbed species are the origins of charges at the heterointerface.[25−35] Identification and control of the charge sources are critical to enable new devices and manipulate their interaction with their surroundings. The modulation of the charge carrier density at the heterointerface was shown to be achieved by ferroelectric gating, control through voltage applied via an atomic force microscopy tip, and mechanical stress applied by using a PFM tip.[2,3,36,37]

Almost universally, processed heterostructures have been exposed to ambient conditions before utilization of all types of characterization techniques including the typical Hall measurements, X-ray photoelectron spectroscopy, and atomic force microscopy except for some work on superlattices or capped films.[34,38] Attempts have been made to clean the surface of adsorbates through ozone cleaning, heating in UHV, and exposing the heterostructure to a flow of nitrogen at elevated temperatures.[30] Even though such techniques may result in a change in the surface adsorbed species concentrations, they do not necessarily form an adsorbate free surface.[30,31] In addition, the fast resaturation of the surface leads to an unknown surface under the fast but uncontrolled transfer of the samples from the cleaning atmosphere to the characterization instrumentation.[31,39] Despite the uncontrolled nature of some of these cleaning techniques, changes provided strong support for the

Received: October 4, 2021
Accepted: December 8, 2021
Published: December 21, 2021

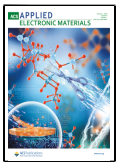

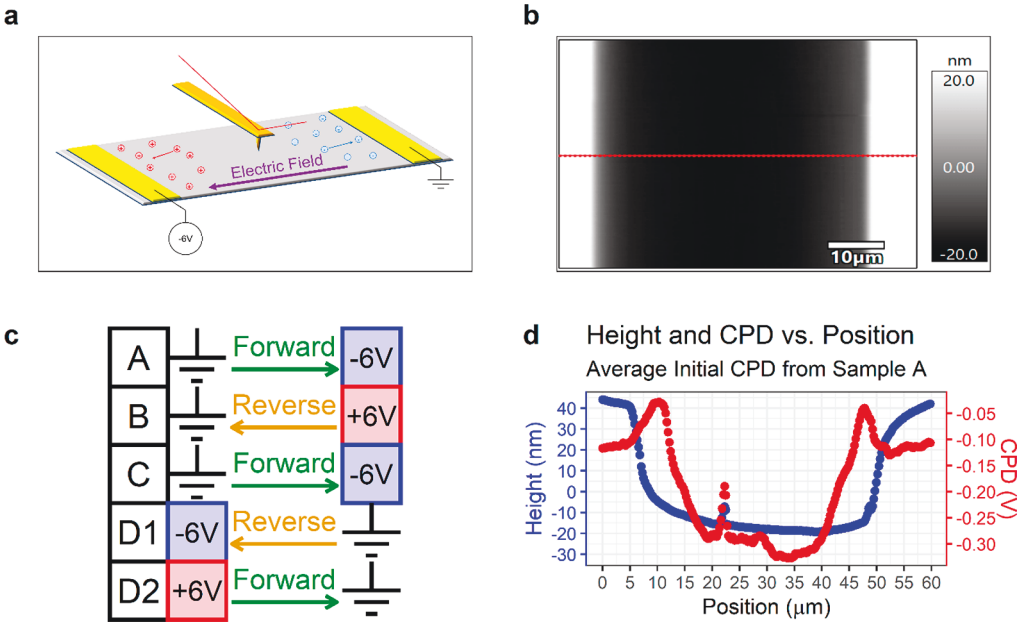

Figure 1. (a) Schematic of the measurement setup. (b) AFM topography for the grounded device with the red line indicating the path of CPD and height measurements. (c) Schematic of cases A, B, C, D1, and D2. The electrode on the left corresponds to ∼0−15 μm while the electrode on the right corresponds to ∼45−60 μm. Forward bias occurs when the electric field flows toward the right, and reverse bias is the opposite. Note that forward and reverse bias are determined by the direction of the electric field and not the value of applied electrical bias. (d) Height profile and average initial CPD before any electrical bias is applied over line on which measurements are taken, shown in red on (b).

effects of surface-adsorbed species on the electrical properties of the interface. Therefore, in this work, the focus is on exposed surfaces saturated with ambient adsorbed species.

Oxygen vacancies (V_O) are described as one of the sources of charge carriers as well as the switchable electromechanical response. Two minima were proposed for the presence of V_O on the surface of the film and at the heterointerface.[25] While migration of V_O can lead to some observations in PFM data, the response of films processed at higher partial pressures is more dependent on the concentration of adsorbed species with Jahn−Teller distortions leading to the PFM observations of hysteresis.[27,29] The V_O concentration at the interface is negligible if the deposition atmosphere was at and above 10^{-4} Torr, which is the processing atmosphere for the films characterized in this article.[23] In addition, both the films just above and below critical thickness showed similar O K-edge EELS patterns near the interface, indicating that the V_O content was low and only depended on the deposition conditions and not the thickness of the film. Thus, the presence of V_O near the interface was not a predictor of the interfacial conductivity.[23] The defect chemistry on the surface and the effects of adsorbed species have frequently been investigated as a function of gate field (i.e., voltage applied through a conductive AFM tip) at magnitudes that cause modulation of charge carrier density at the heterointerface (e.g., tuning). The presented work here focuses on the characterization of the surface of the films with insulating heterointerfaces. Neither KPFM nor tr-KPFM includes application of gate voltage that would change the interfacial behavior. The film of interest is 3 u.c. (unit cell) thick—just below the critical thickness—deposited at 750 °C under a 10^{-4} Torr O_2 atmosphere on a Ti-terminated $SrTiO_3$ substrate. Our films exhibited critical thickness at the same point as most in the literature where the heterointerface for the 3 u.c. thick film is insulating and 4 u.c. thick film is conducting. The critical thickness can depend on the chemical potential of the oxygen (and hydrogen) and is a function of surface defect density. This indicates that the film studied in this work has comparable surface defect density to other films studied in the literature.

The exposed surface of the films contains both carbonaceous species and dissociated water molecules.[31] There have been reports on adsorbed polar water molecules that align on the surface, affecting the interfacial properties, but calculations and other experimental work indicated that water is more likely to be dissociated on the surface.[40−43] It is this dissociated water molecule, with H^+ attached to a surface oxygen and OH^- attached to a surface cation, that is believed to be a major factor in both the origin of charge carriers and the change in their concentration under gate fields applied by AFM tip.[30,35,40] Calculations show that H^+ on the surface results in substantial doping of the heterointerface, and the surface coverage extends between a half to a full monolayer of hydrogen on the surface.[35,40] However, the carrier density would decrease if other acceptor species (such as OH^- or other O^-, O_2^-, and O_3^- species that may be introduced during plasma cleaning) also exist.[30] The breaking of the bond at Al−OH or at AlO−H requires very high energies that cannot be achieved either by heating in UHV, even at 1000 °C, or by solvent cleaning.[30,31] Thus, the presence of oxygen species on the surface results in trapping electrons from other donors on the surface. Therefore, understanding of the surface adsorbed species kinetics is crucial to control the coupled interface conductivity. The relative amount of different adsorbed species, for example H^+ and OH^-, can change based on the surface V_O. Thus, the surface V_O can have an indirect effect on interface conductivity by varying the ratio of donor H^+ and acceptor OH^-. In this indirect effect, the OH^- would annihilate the surface V_O and act as a surface oxygen with H^+ attached. Because first-principles calculations showed that

https://doi.org/10.1021/acsaelm.1c00954
ACS Appl. Electron. Mater. 2022, 4, 206−216

the formation of a conducting interface is due to surface adsorbed species (i.e., H^+), it would not have thickness dependence and thus would result in metallic interfaces below the critical thickness. However, the V_O formation energy on the surface of the film decreases with increasing thickness due to the dipolar field.[44] The imbalance created in the H^+/OH^- ratio due to surface V_O then can result in the observation of a critical thickness, emphasizing again the motivation for investigating surface-adsorbed species. Note that the increase in the VBM for a LAO surface with adsorbed species coverage may not be high enough to close the gap with the CBM of the STO until the critical thickness, providing another path to formation of critical thickness. Surface V_O were also suggested to have direct contribution to the interface charge carrier density as well as its tunability if they diffuse across the thickness of the film under external drives such as electric field or mechanical stress.[26,36,45] On the other hand, some calculations showed lower formation energy for Al adatoms than surface V_O, which can still lead to similar interfacial observations where Al donates $3e^-$ per adatom.[33] Note that other oxygen sources on the surface such as carbonaceous species were found to be less likely to contribute to the interfacial behavior and are easier to remove.

Herein, we focus on the lateral transport dynamics using Kelvin probe force microscopy (KPFM) and time-resolved KPFM (tr-KPFM). In KPFM, the measured contact potential difference (CPD) is related to the work function difference between the metal tip and the sample, if metallic. For semiconductor/insulating samples, band bending, dopant density, surface charge density, and density of surface states can all contribute to the measured CPD. Time resolution allows determination of the dynamic behavior on the surface which here we apply to understanding the surface of LAO/STO heterostructure that is closely coupled with its heterointerface.

MATERIALS AND EXPERIMENTAL PROCEDURE

For local transport measurements in this study, two Ni electrodes were deposited laterally on the LAO/STO surface with a channel distance of 50 μm (Figure 1a). The choice for 50 μm was primarily based on the capabilities of the equipment. It is desirable for the AFM scan to be large enough so local flaws do not prevent accurate data analysis, but the channel width cannot be too large as to distort measurements for the given range of the scanning probe. Shown in Figure 1b is an image of AFM topography for the grounded device. The film was 3 u.c. thick, which is just below the critical thickness. Films are grown via pulsed laser deposition following the conditions summarized elsewhere.[23,24] To study the spatial variation of the potential distribution during application of an electric field, KPFM profiling was performed across a single X-scan profile by disabling the Y-scan motion of the AFM scanner while different biases were applied across the device. The spatial resolution of the lateral surface potential mapping is on the order of the tip radius, which is ~20 nm. The mode of KPFM we used was frequency-modulated heterodyne KPFM. This method has recently been shown to provide the most quantitative potential measurements on lateral devices. Axt et al. showed that FM heterodyne KPFM[46] had the best performance, capturing 99% of the potential difference across a model lateral device structure and was largely free from crosstalk due to the presence of strong stray fields, which hamper many other KPFM modalities (Figure S1). This operation was comparable to FM-KPFM and far superior to traditional AM-KPFM.[47]

Each applied bias has a data set, which is a collection of CPD measurements taken for 256 positions along the 60 μm system every 2 s. The different electrical bias cases are (A) −6 V, (B) +6 V, (C) −6 V, and (D1) −6 V immediately followed by (D2) +6 V in the same run. For case D, the ground was switched to the opposite pad from cases A−C. Another important aspect of each case is the bias or electrical field direction. Forward bias, electrical field going from position 0 to position 60 or left to right, and reverse bias, electrical field going from position 60 to position 0 or right to left, denote such directions (Figure 1c). The voltage of ±6 V over a 50 μm channel corresponds to an estimated electric field of 1.20 kV/cm. This approximation is complicated by the interdigitated electrodes, as opposed to parallel plates. More accurate calculations of the electric field on ferroelectrics in such device configurations would require analytical modeling, but the 1.20 kV/cm estimation is adequate for our purposes.[48] The orientation and placement of the film do not change between cases. For cases A−C, CPD was measured for 60 s after the field was applied (bias-on or "polarization") and continuously measured for 238 s after the field was removed (bias-off or "relaxation"). For case D1, polarization was 74 s while relaxation was 138 s. For case D2, polarization was 60 s while relaxation was 192 s. In total, there are 256 separate fits per sample, one for each position. For polarization, there were 30 points for each fit for cases A−C and D2. For case D1, there were 37 points. For relaxation, there were 119 points for cases A−C, 69 for case D1, and 96 for case D2. It will be shown that the times allotted for both polarization and relaxation are adequate for the systems to reach full stability. The time stamp at which the bias is first applied is defined as t = 0 s, and polarization measurements are captured for t = 2−60 s for cases A−C. Cases D1 and D2 have different time periods because of their unique duration of polarization or shift in time due to continuous collection of two separate cases. t < 0 s indicates data collection prior to the application of bias.

All KPFM measurements were performed on an Asylum Research MFP 3d platform by using as-received Pt/Ir-coated (Nanosensors, PPP-EFM) AFM probes, with a nominal mechanical resonance frequency and spring constant of 75 kHz and 2.8 N/m, respectively. Measurements were performed by using FM-heterodyne KPFM.[46,47] The topography was captured by using amplitude modulation (AM) on the first cantilever eigenmode, and the oscillation amplitude was kept to ~60 nm operating in an attractive regime. For the heterodyne KPFM measurements, we used a Zurich Instruments HF2LI for signal demodulation and bias feedback, and the nulling bias was supplied to the tip. The electrical drive voltage was applied at frequency ω_e, corresponding to the first cantilever eigenmode frequency minus the fundamental eigenmode frequency ($\omega_e = \omega_1 - \omega_0$). The sideband detection was performed at ω_1.

RESULTS AND DISCUSSION

Changes in the CPD can be due to the changes in work function of the material, chemical dipoles on the surface, and surface charging by injected charges, oxygen vacancies, or surface-adsorbed species, specifically dissociated water.[49−52] It is reasonable to suggest that the CPD image for the grounded device effectively describes the static potential distribution across the device (Figure 1b). Further influences due to the water layer, surface contaminants, and so on can also influence the absolute measured CPD. For example, other KPFM CPD results in the literature demonstrated an increase in work function when a conducting interface was converted to an insulating one through a surface plasma treatment that introduced electron getters even for films above the critical thickness.[30] The drop in work function under applied voltage modifying the interface from an insulating one to a conducting one is a function of the atmosphere; for example, CPD increased moving from air to oxygen (with H_2/N_2 to oxygen also providing similar changes). Such an atmosphere dependence indicates complicated contributions from adsorbed species, redox reactions, and electrochemical components.

Our measurements show large CPD values for the films with thickness below t_c and exposed to ambient air at room

https://doi.org/10.1021/acsaelm.1c00954
ACS Appl. Electron. Mater. 2022, 4, 206−216

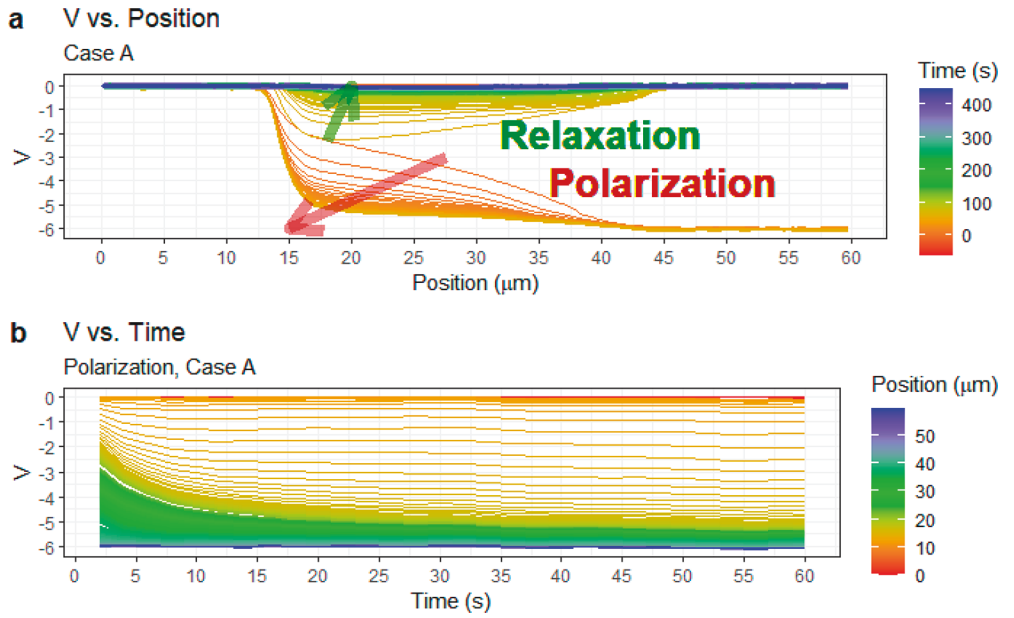

Figure 2. (a) Surface voltage as a function of position with each line representing a different time for polarization and relaxation. The brown arrow indicates increasing time for polarization while the green arrow indicates increasing time for relaxation, which occurs immediately after polarization. The red lines for $t < 0$ s are covered by the blue lines for $t > 400$ s, which are all constant at 0 V. (b) Surface voltage as a function of time with each line representing a different position during polarization. Positions ∼0−15 μm (red lines) and ∼45−60 μm (blue lines) correspond to electrodes, and the surface voltage of these regions shows no change over time as expected.

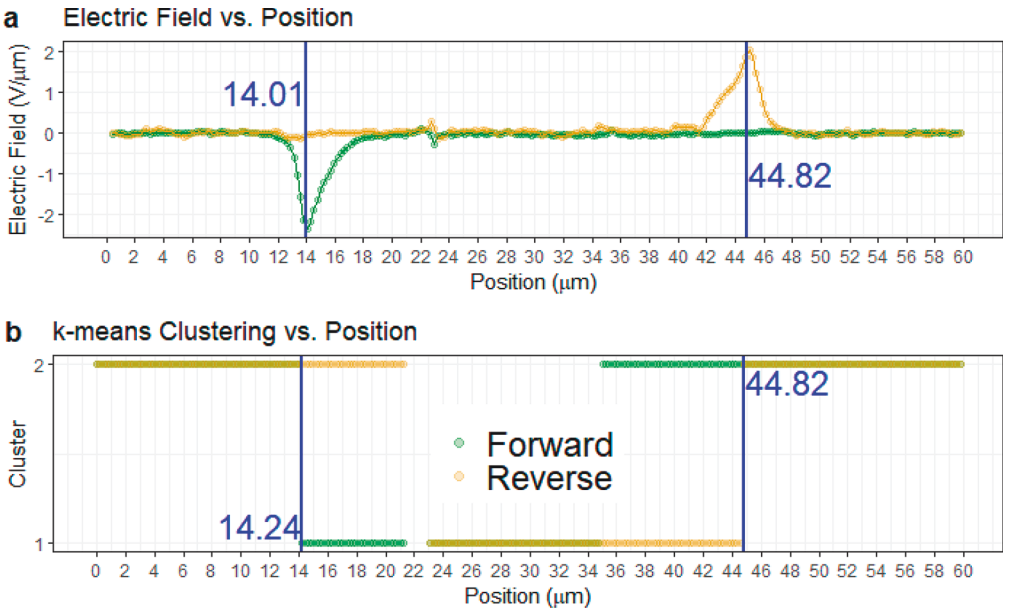

Figure 3. Determination of boundaries between film and electrode using (a) maximum electric field and (b) *k*-means clustering on the profile of polarization curves for both forward and reverse bias. These two methods yield agreeing results, and the electric field boundaries will be universally used in this study.

temperature (∼20 °C) and 30−40% relative humidity, consistent with observation of higher CPD with higher resistivity of the interface (Figure 1d). The CPD was measured before every run and did not show any significant change between cases A−D (Figure S2). A potential barrier was observed at the interfaces with electrodes. Note that this is not the potential barrier between the electrode and the film but the barrier on the surface. Similar electrode schemes on films that are above the critical thickness (5 u.c.) showed ohmic contacts during the measurement of interface conductivity. Topological analysis shows electrode edges that are not perfectly sharp, indicating some diffusion underneath the mask during evaporation. A very narrow surface artifact, a possible dust particle on the surface, was observed and removed from further analysis (Figure S3). The rest of the surface profile of the channel was smooth. A small change in CPD, ∼43 mV, was observed around the 30 μm point (Figure 1d), but further inspection shows there are no topographical discrepancies associated with this area (Figure S4).

Figure 2a shows both the polarization and relaxation results for case A when bias (−6 V) was applied on a saturated surface (i.e., aged in an ambient atmosphere). The measured CPD

https://doi.org/10.1021/acsaelm.1c00954
ACS Appl. Electron. Mater. 2022, 4, 206−216

profile at 0 V was used to normalize the potential profiles (i.e., $V = V_{cpd}(V_{bias}) - V_{cpd}(0)$), effectively removing offsets due to the work function difference between the tip and sample, such as influences due to water layer/adsorbates in the original surface, and the work function difference between the electrode and the channel, thus isolating changes associated with the applied source−drain voltage (Figure 2a). We note, at the biased electrode, the normalized potential matches the applied device bias, thus validating the CPD correction procedure to solely analyze changes in surface voltage (V). The largest potential drop was observed at the higher-potential, more positive electrode (>5 V). The potential was seen to be almost uniform across the channel.

To investigate relaxation mechanisms, the data are converted to surface voltage versus time for each position for polarization (Figure 2b). There is relatively smooth polarization/relaxation for positions in the middle of the device, which represent the channel. Conversely, positions on the end, where the electrodes are, show little to no polarization/relaxation, as expected. To analyze the film, boundaries between film and electrode must be defined, but these exact boundaries are not immediately obvious. As mentioned before, topological analysis shows electrode edges that are not perfectly sharp, indicating some diffusion underneath the mask during evaporation (Figure 1d). However, a sharp potential drop occurs at this interface (Figure 2a) during polarization. Therefore, the position with maximum electric field ($E_{field} = dV/dX$) is interpreted as the interface (Figure 3). As the potential drop mainly occurs at the higher-potential electrode, to determine both interfaces, both the forward (case A, electric field moving from position 0 to position 60 or left to right) and reverse bias (case B, electric field moving from position 60 to position 0 or right to left) cases were used (Figure 3a). This approach uses the surface voltage as a function of position for a given time (here 60 s is used because the system is fully stable), and the positions of interfaces were determined to be 14.01 and 44.82 μm. The position of the interface based on electric field maximum does not depend on the magnitude of the bias.

To support this interpretation, a clustering approach was also employed on the time polarization curves, which essentially used the time dependence of surface voltage at different positions during polarization. The curves were all normalized to start at zero so they could be clustered based on their profile rather than on their absolute values. The elbow method and silhouette method were used to determine the optimal number of clusters for each data set. The elbow method finds the "elbow" on the graph after the fviz_nbclust() function (package "factoextra" ver. 1.0.7) in R is used with the method "total within sum of square". The silhouette method directly determines the optimal number of clusters with the same function but with method "silhouette". Both approaches identified two clusters as the optimal amount for all data sets. The k-means clustering was conducted with the kmeans() function in R (package "stats" ver. 4.0.2) seeding two centers. The use of k-means clustering defined boundaries between film and electrode and produced results that are close to or exactly the same as the maximum electric field positions when applied to the same interface for forward (14.24 μm) and reverse bias (44.82 μm) (Figure 3b). Therefore, both the potential drop as a function of position and the time dependence of surface voltage change provided interface positions that are supportive of each other, and from here on, the positions with the maximum in electric field will be used as the position of the electrode/channel interface, and analysis on the time relaxation curves will focus on the channel area as defined by these borders. On the side with lower potential, for both forward and reverse bias, some of the channel is clustered with electrodes, indicating that the applied bias does not significantly affect polarization curves in that region of the channel.

A polarization/relaxation time constant (τ) can be determined to be a function of position from each of the curves in Figure 2b by using $f(t) = A + Be^{-t/\tau}$. The approach of using an exponential decay model and derived time constants to describe the change in surface voltage has proven successful in characterizing surface dynamics in similar studies, and it is assumed that similar mechanisms and chemistries are present in this study.[53−55] A second time constant can also be introduced via $f(t) = A + Be^{(-t/\tau_1)} + Ce^{(-t/\tau_2)}$. This additional term is empirically driven and can improve the overall goodness of fit of the model by describing different parts of the data separately. Using a second relaxation term is a novel method for this application. The parameter A is the vertical offset in the surface voltage, which represents the equilibrium potential after polarization or relaxation is complete. The pre-exponential parameters B and C represent the maximum drop in potential for each species over the polarization and relaxation periods. The time constant (τ) is the mean lifetime of charge transport and is inversely proportional to the diffusion constant.[53] The τ for the one-term model captures the mean lifetime of all mobile species while the τ's for the two-term capture fast- and slow-moving species separately.

In certain positions, at greater times, polarization or relaxation was completed before the end of data collection, and a plateau was observed (i.e., no statistically discernible change in surface voltage). These plateaus were filtered away as they do not contribute to the polarization or relaxation mechanism (Figure S5), and this process increased the quality of time constant analysis (Figure S6).

Using the nls( ) function in R (package "stats" ver. 4.0.2), we fit polarization and relaxation curves with a single and double time constant with R estimating all three (A, B, and, τ) and five (A, B, C, τ_1, and τ_2) parameters, respectively. Because the two-exponential-term model is more complex, it converges only on a narrower range of data; hence, it fits to fewer curves than its simpler one-term counterpart.

The physical interpretations of the fitting parameters agree with the original data. The A parameters align with the equilibrium potential (t = 60 s, shown in Figure S7) while $A + B$ or $A + B + C$, depending on which model is being considered, represent the surface voltage at $t = 0^+$. The data on which the models were fit started at t = 2 s, and the sum of the parameters plotted with surface voltage at t = 2 and 4 s as a function of position show even spacing between lines, suggesting that the sum of the parameters is an accurate simulation of the surface voltage at the instant bias is applied (Figure S8). In addition, the sign and profile differences of A show the distinction between forward and reverse bias as well as the value of the applied bias. For example, reverse bias (case B) and forward bias (case D2) have the same sign for parameter A because the applied bias is the same for both (+6 V) but applied to opposite electrodes (Figure S9).

After fitting one- and two-term models to all cases for polarization and relaxation, it was found that results were consistent for a given applied bias or bias direction. This indicates that a sample aged in atmospheric conditions (case

https://doi.org/10.1021/acsaelm.1c00954
ACS Appl. Electron. Mater. 2022, 4, 206−216

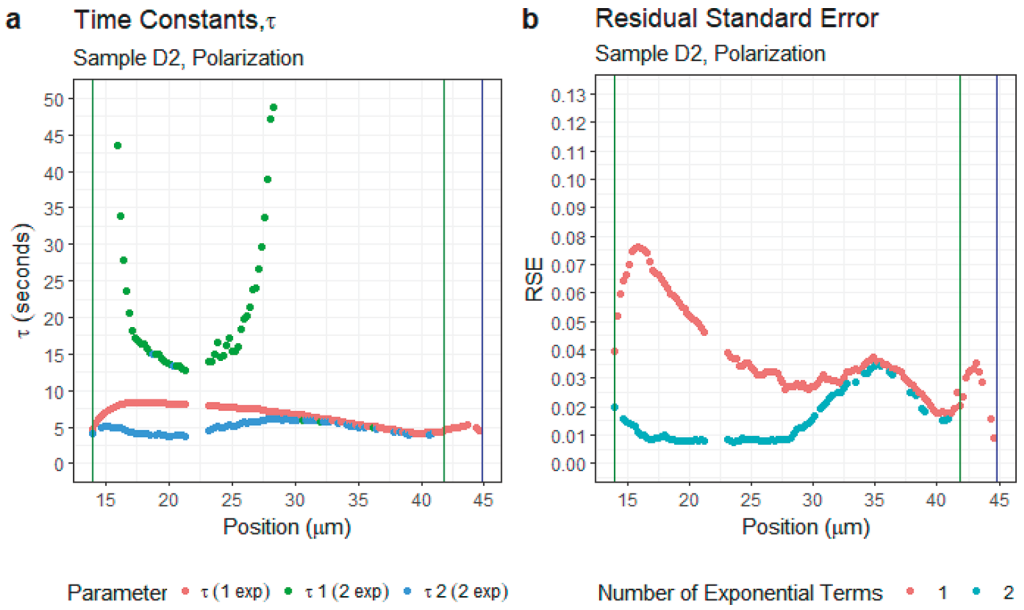

Figure 4. (a) Time constants, τ, for one- and two-term models and (b) the associated RSE for each model. These models are for case D2 (+6 V forward bias) polarization. Here, the addition of a second time polarization term in modeling improves the fit, suggesting there are multiple, distinct polarization mechanisms. The blue vertical lines indicate the boundary between film and electrode as determined by the maximum electric field. The green vertical lines indicate the clustering boundaries determined specifically for case D2, which tend to capture the active region of charge movement but seem to have extended beyond that for this situation. The active region generally ends where the one- and two-term models begin to converge.

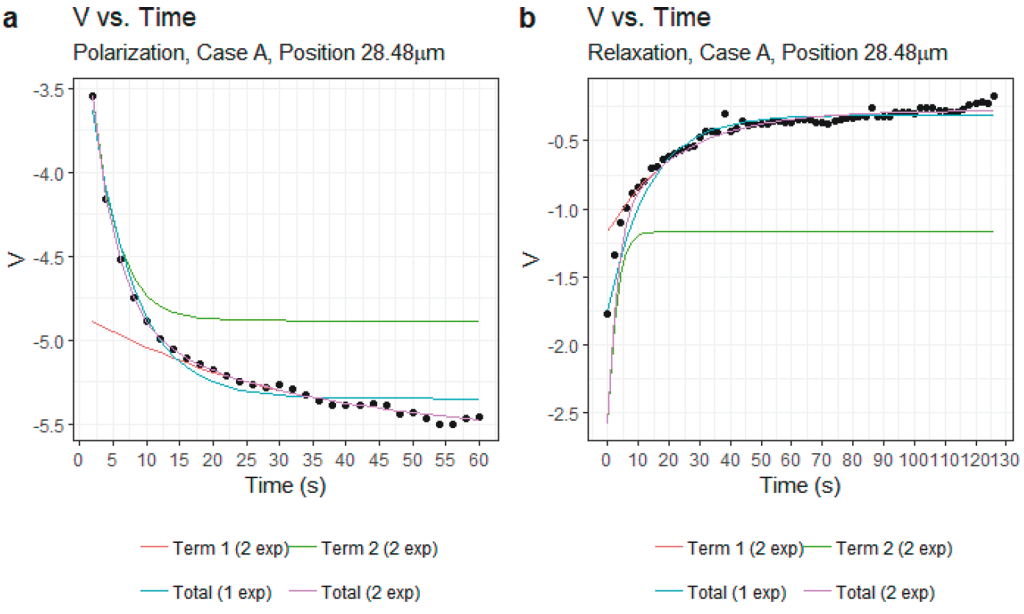

Figure 5. Cleaned data for case A for (a) polarization and (b) relaxation with the one-term model, the two-term model, and each component of the two-term model individually. Each component of the two-term model is vertically shifted to align with the data points that it describes for this visualization.

A) behaves no different than one with a recent electrical history (cases B–D) and that forward and reverse biases lead to symmetric results. The discussion will focus on the results for cases D1 and D2 because they had the cleanest data and produced accurate models for a wider range of positions along the channel than cases A–C but still closely represented the behavior for all these cases.

Residual standard error (RSE) in case D2, under forward bias at +6 V, indicates that two time constants enhance the characterization of the polarization mechanisms, one with faster kinetics (τ_2 in the range 4–6 s) and the other with slower kinetics. The improved RSE with two models is shown in Figure 4 while Figure 5 shows how both a fast and slow time constant describe different parts of the data and how a single term cannot capture both dynamics fully. This development is empirical but could be associated with multiple mechanisms contributing to the surface processes as have been found in other studies.[35,39−42,45] The single polarization fit captures the faster kinetics with a slight increase in the relaxation times (i.e., around 6–8 s) and greater RSE as it tries to accommodate for

https://doi.org/10.1021/acsaelm.1c00954
ACS Appl. Electron. Mater. 2022, 4, 206−216

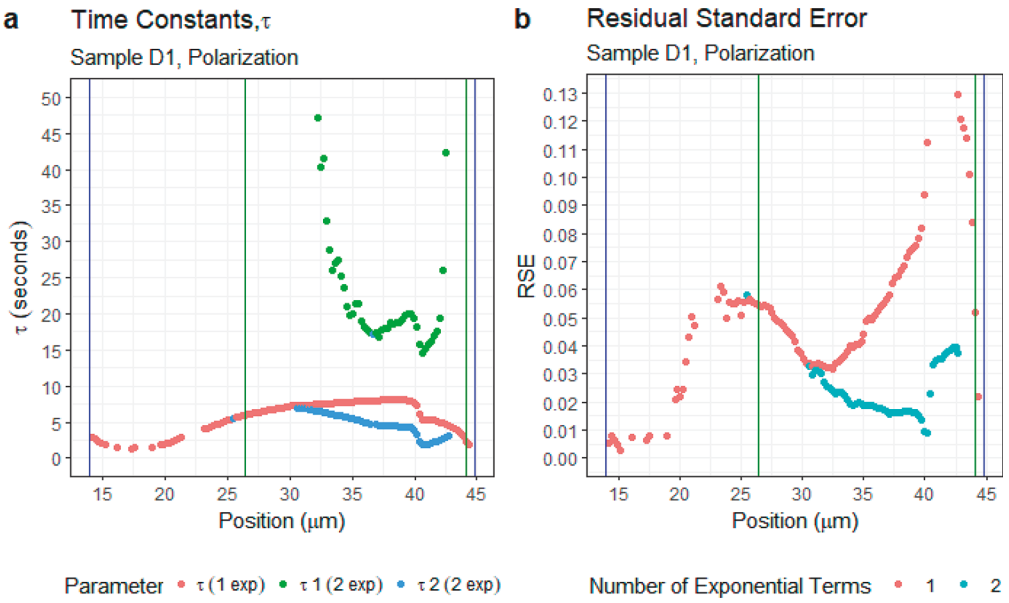

Figure 6. (a) Time constants, τ, for one- and two-term models and (b) the associated RSE for each model. These models are for case D1 (−6 V reverse bias) polarization. Here, the addition of a second time polarization term in modeling improves the fit only for a smaller area than for case D2, but the slower term is significant for an approximately equal area. The blue vertical lines indicate the boundary between film and electrode as determined by the maximum electric field. The green vertical lines indicate the clustering boundaries determined specifically for case D1, which capture the active region of charge movement.

the slow relaxation at higher times. The fitting of two polarization mechanisms converged over most of the channel, but the RSEs of one- or two-time-constant fits started to merge around 32 μm just as the one-term τ started to merge with τ_2, indicating that the slower mechanism was no longer active, and polarization could be explained simply with one term beyond this point. This supports the theory that the area of the channel away from the higher-potential electrode is not affected by this second polarization mechanism. While the faster mechanism did not show any significant dependence on the position along the channel, the slower mechanism had significant change in polarization time with position, maximizing near the interface and furthest from the interface (in the discernible range). The increase in polarization time near the interface indicates a reaction beyond diffusion of surface species. The increase in time constant for the slower mechanism toward the center of the channel is likely a result of the model fitting process trying to mathematically create a second term where there is little happening in the physical system. The associated pre-exponential parameter for the slower term, B, rapidly decreases in magnitude as τ_1 increases, meaning the entire term is being driven toward zero and is no longer significant (Figure S10a). The slower time constant, τ_1, only represents a legitimate mechanism or reaction between the higher-potential electrode and the position in the middle of the channel when its values begin to spike while the faster time constant, τ_2, is valid for nearly the entire channel.

Under reverse bias for −6 V (case D1), defining two polarization mechanisms improved the RSE mainly close to the electrode with higher potential (Figure 6). All polarization behavior was similar to what is observed for forward bias. For the two-term model, the fast polarization time ($\tau_2 \approx 3-6$ s) merged with that of single polarization curve fit away from the higher-potential electrode into the channel as the RSEs also merged. The slower polarization showed a similar maximum near the higher-potential electrode and deepest into the channel where the fits still converged for two polarization times. Again, this second maximum toward the center of the channel is no longer mathematically significant, as shown by its associated pre-exponential parameter B (Figure S10b). It is interesting to note that the fit for two polarization times stopped converging or became nearly identical with the one-term model near 30 μm, which is approximately the center of the channel. This demonstrates the symmetry of the physical system, which is further supported by results from cases A−C (Figures S11−S13).

On the basis of these results, we can conclude the following: (i) There are two diffusion processes, where the fast one covers the whole channel with polarization time of $\tau_2 \approx 3-6$ s. (ii) The slow diffusion process ($\tau_1 \approx 10-20$ s), further slowing ($\tau_1 \approx 40-50$ s) near the higher-potential electrode, covers a limited area of the channel extending from said electrode.

The clustering techniques described earlier identify an "active area" in the film closer to the higher-potential electrode where there is significant charge mobility.[56] The one-term model fits for positions outside of this region for some samples where it is likely that only the fast-moving species are active. This is supported by the fact that the one-term τ decreases outside of the active area to values in the range of the lower τ for the two-term models. Regardless of bias direction or which electrode is grounded, the active area, as defined by the clustering or approximately where the one- and two-term models begin to merge, is consistently around 21−25 μm in length. This consistency is expected for constant bias magnitude as only ambient conditions like relative humidity and temperature affect the size of this region.[56]

The fast-moving species has a polarization time consistent with those found for similar studies of ceria (CeO_2),[54] $LiNbO_3$,[55] and Ca-substituted $BiFeO_3$,[53] which all identified protons, hydroxyl groups, and/or electrons from dissociated water molecules as the charge carriers for the conditions used in this study (room temperature). The diffusivity D can be

https://doi.org/10.1021/acsaelm.1c00954
ACS Appl. Electron. Mater. 2022, 4, 206−216

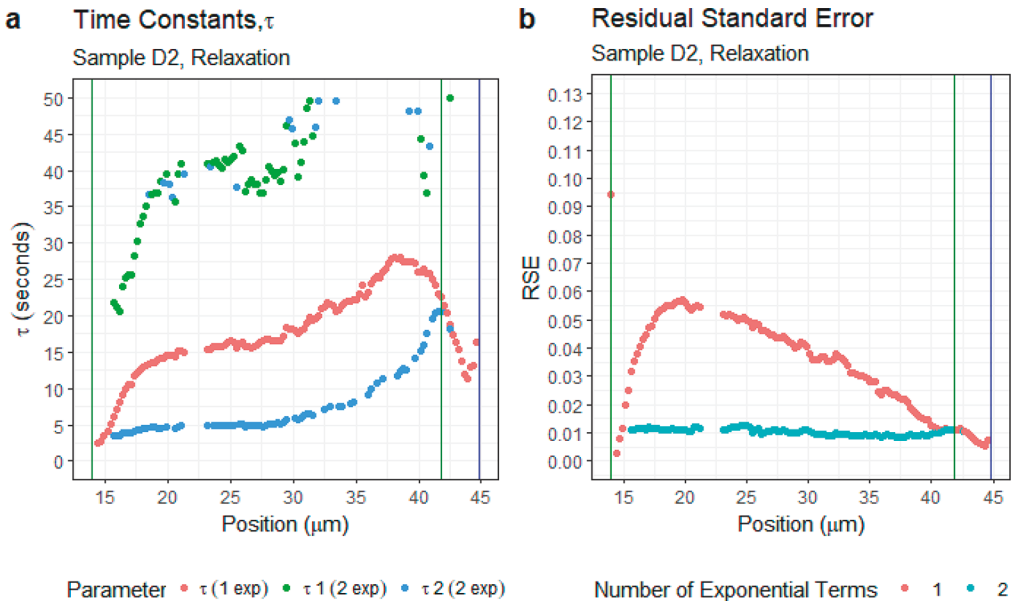

Figure 7. (a) Time constants, τ, for one- and two-term models and (b) the associated RSE for each model. These models are for case D2 (+6 V forward bias) relaxation. Here, the addition of a second time relaxation term in modeling improves the fit, showing that different relaxation mechanisms are reproducibly observed. The blue vertical lines indicate the boundary between film and electrode as determined by the maximum electric field. The green vertical lines indicate the clustering boundaries determined specifically for case D2.

determined by the time constant τ and distances covered by the mobile species d, which can be approximated as the channel width for the fast-moving species, by using the equation $D = \frac{d^2}{\tau}$.[53] For the fast-moving species, $D = \sim(2-3) \times 10^{-10}$ m/s^2, which approaches the diffusivity of protons in water at room temperature at $\sim 10^{-8}$ m/s^2.[43,53] The H^+ ions would be moving in the same direction of the electric field from higher to lower potential.

Several mechanisms have been proposed to explain the water dissociation on oxide films under an applied electric field with some centered around reactions happening at or near a triple-phase boundary (TPB) of film, electrode, and atmosphere.[54,56] The rapid increase in τ_1, the slower time constant, near the higher-potential electrode at the edge of the channel may be a product of such a reaction at the TPB. Similar increases in τ at the edge of the channel were observed by Strelcov et al. for a Ca-substituted $BiFeO_3$ thin film.[53]

The slower-moving species ($\tau_1 \approx 10-20$ s or $\tau_1 \approx 40-50$ s) are likely hydroxide molecules moving in the opposite direction of the electric field with the higher time constant range capturing a reaction at the TPB. The possibility that this higher time constant represents other surface adsorbed species also exists. While the charge transport through oxygen vacancies is possible, it is unlikely that they would make a significant contribution at room temperature and a relatively low applied bias.[53] The more likely role of oxygen vacancies in these conditions is acting as a catalyst in water splitting reactions.[56] The contributions of the fast- and slow-moving species to the potential drop can be compared by their pre-exponential terms (parameters B and C). The ratio of parameter C (fast) to parameter B (slow) during polarization is within the range of ~1−3:1 in the active region, with cases A, C, and D1 (all −6 V) staying consistently >2:1 in the active region (Figure S14a). This demonstrates the dominance of the fast-moving species in charge redistribution.

When the bias is removed in each case, there is a relaxation observed. The change in CDP is <2 V, so the modeling results are a little noisier compared to the corresponding polarization cases. When the same approach is applied to the bias-off or relaxation data, in case D2 (forward bias), two relaxation times provided a better fit than one relaxation term for nearly the entire channel, but time constants begin to increase outside of the active areas seen in polarization (Figure 7). The fast relaxation time (≈ 3−6 s in the active area) is consistent with fast polarization. The slow relaxation time is higher for relaxation than polarization, and while it smoothly increases moving away from the higher-potential electrode, it does not have any sudden spikes like it did during polarization. In addition, the one-term model stays consistently between the fast and slow time constants without merging with either, indicating that one relaxation mechanism does not begin to dominate the other.

Similar results for relaxation were found for the other cases with the models converging for larger areas, the fast time constants agreeing with those during polarization and the slow time constants being greater than those of polarization while steadily increasing moving away from the higher-potential electrode rather than spiking (Figures S15−S18). It was similarly found that the slower time constant represents a significant process for most of the channel. This is further supported by the ratio of parameter C to parameter B for relaxation, which is consistently lower than it was during polarization (Figure S14b). The similarity between the fast time constants for polarization and relaxation indicates that proton movement is what is being captured. While during polarization the slow time constant is likely associated with a reaction near the higher-potential electrode and movement of hydroxide ions, during relaxation it is probably something different; a redistribution of hydroxide ions that is happening slower than it did during polarization is possible, but there could be other processes as well. The main mechanism behind the slower time constant may be the reabsorption/resaturation

https://doi.org/10.1021/acsaelm.1c00954
ACS Appl. Electron. Mater. 2022, 4, 206−216

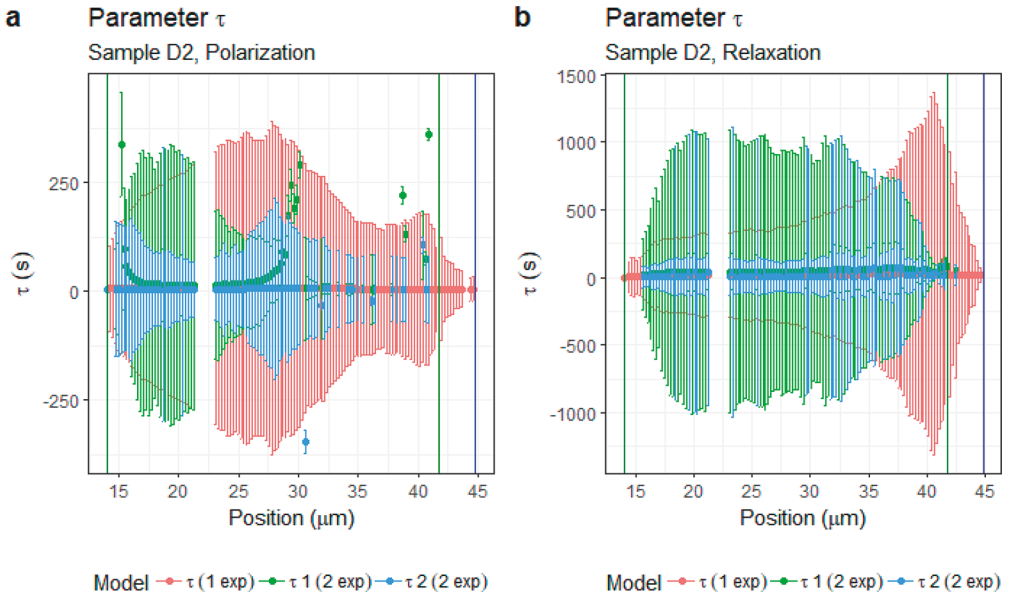

Figure 8. Time constants with error for case D2 for (a) polarization and (b) relaxation. The error bars show the standard error.

of moisture on the surface from the atmosphere. Because the slower time constant is significant along most of the channel and does not spike at all, it may be the same process happening everywhere on the film. The steady increase in this time constant moving away from the higher-potential electrode could represent the same reaction happening at slightly different rates with that rate being controlled by the magnitude of the potential drop at each position along the film.

Investigation of the error of the individual parameters of the models found that the standard error for the terms *A* (vertical shirt), *B* (pre-exponential term), and *C* (pre-exponential term) were very small while those for the time constants were rather large. All samples demonstrate these same patterns at an approximately equal magnitude, so the errors for one sample are representative of the other samples. The error for parameters *A*, *B*, and *C* for case D2 are shown in Figures S19 and S20. The error for the time constants for case D2 is shown in Figure 8. The discussion regarding the magnitude of the time constants and the associated mechanisms were related to the literature where the results were also based on the overall fit and where individual errors for each parameter were not available.[53−55] While it is clear that there is a fast and a slow contribution to the overall behavior (Figure 5), the exact magnitudes of time constants are less certain.

CONCLUSIONS

The surface of LAO/STO heterostructures was investigated with tr-KPFM under a bias across the surface. The time dependence of the changes associated with polarization (bias-on) and relaxation (bias-off) has been observed and was shown to be dependent on the position within the channel. Aging or electrical history was shown to not affect the observations, indicating fast stabilization of the surface within the environment. The time constants that were derived from the surface voltage measurements were consistent between cases for a given bias state (polarization or relaxation). The values of the applied bias (±6 V) and bias direction (forward or reverse) also did not change results and were symmetric about the center of the channel. During polarization, it was found that in the active area near the higher-potential electrode results could be associated with two diffusion processes based on the literature. The faster one, having a time constant of ∼3−6 s, is likely correlated to the transport of H^+ ions and happened over nearly the entire film. The slower term is ∼40−50 s close to the higher-potential electrode where it may indicate a reaction, such as the dissociation of water, happening at a TPB. This slower term then decreases to ∼10−20 s moving toward the middle of the film where it may represent the transport of OH^- ions, and it does not contribute to the time-dependent changes outside of the active area. During relaxation, similarly, results could be associated with two processes happening. The faster relaxation term was similar to that of the faster polarization term and was related to the movement of H^+ ions. The slower relaxation term was different than the slower polarization term in that it covered the whole channel and exhibited a gradual increase moving away from the higher-potential electrode. In addition, it had larger values. The slower process during relaxation is different than that during polarization, and during relaxation, it could represent a slower diffusion of OH^- ions or the reabsorption/resaturation of moisture from the environment.

ASSOCIATED CONTENT

Supporting Information

The Supporting Information is available free of charge at https://pubs.acs.org/doi/10.1021/acsaelm.1c00954.

Additional experimental results and figures and descriptions of data (PDF)

AUTHOR INFORMATION

Corresponding Author

Hugh Smith − *Department of Materials Science and Engineering, Case Western Reserve University, Cleveland, Ohio 44106-7078, United States;* orcid.org/0000-0002-8466-2401; Email: hbs35@case.edu

Authors

Liam Collins − *Center for Nanophase Materials Sciences, Oak Ridge National Laboratory, Oak Ridge, Tennessee 37830-6286, United States;* orcid.org/0000-0003-4946-9195

https://doi.org/10.1021/acsaelm.1c00954
ACS Appl. Electron. Mater. 2022, 4, 206−216

Alp Sehirlioglu − *Department of Materials Science and Engineering, Case Western Reserve University, Cleveland, Ohio 44106-7078, United States;* orcid.org/0000-0002-9708-4049

Complete contact information is available at: https://pubs.acs.org/10.1021/acsaelm.1c00954

Notes

The authors declare no competing financial interest.

■ ACKNOWLEDGMENTS

Characterization of the heterostructures with tr-KPFM was conducted at the Center for Nanophase Materials Sciences, which is a DOE Office of Science User Facility. H.S. and A.S. acknowledge financial support from NSF Career Award (award #1749440). H.S. thanks the Case Western Reserve University SOURCE (Support of Undergraduate Research & Creative Endeavors) office for a STEM Summer Research Fellowship.

■ REFERENCES

(1) Ohtomo, A.; Hwang, H. Y. A High-Mobility Electron Gas at the $LaAlO_3/SrTiO_3$ Heterointerface. *Nature* **2004**, *427* (6973), 423−426.
(2) Thiel, S.; et al. Tunable Quasi-Two-Dimensional Electron Gases in Oxide Heterostructures. *Science* **2006**, *313* (5795), 1942−1945.
(3) Cen, C.; Thiel, S.; Hammerl, G.; Schneider, C. W.; Andersen, K. E.; Hellberg, C. S.; Mannhart, J.; Levy, J. Nanoscale Control of an Interfacial Metal-Insulator Transition at Room Temperature. *Nat. Mater.* **2008**, *7* (4), 298−302.
(4) Cen, C.; Thiel, S.; Mannhart, J.; Levy, J. Oxide Nanoelectronics on Demand. *Science* **2009**, *323* (5917), 1026−1030.
(5) Mannhart, J.; Blank, D. H. A.; Hwang, H. Y.; Millis, A. J.; Triscone, J.-M. Two-Dimensional Electron Gases at Oxide Interfaces. *MRS Bull.* **2008**, *33* (11), 1027−1034.
(6) Kalabukhov, A. S.; Boikov, Yu. A.; Serenkov, I. T.; Sakharov, V. I.; Popok, V. N.; Gunnarsson, R.; Börjesson, J.; Ljustina, N.; Olsson, E.; Winkler, D.; Claeson, T. Cationic Disorder and Phase Segregation in $LaAlO_3/SrTiO_3$ Heterointerfaces Evidenced by Medium-Energy Ion Spectroscopy. *Phys. Rev. Lett.* **2009**, *103* (14), 146101.
(7) Verbeeck, J.; Bals, S.; Kravtsova, A. N.; Lamoen, D.; Luysberg, M.; Huijben, M.; Rijnders, G.; Brinkman, A.; Hilgenkamp, H.; Blank, D. H. A.; Van Tendeloo, G. Electronic Reconstruction at N-Type $SrTiO_3/LaAlO_3$ Interfaces. *Phys. Rev. B: Condens. Matter Mater. Phys.* **2010**, *81* (8), 085113.
(8) Wei, W.; Sehirlioglu, A. Strain Relaxation Analysis of $LaAlO_3/SrTiO_3$ Heterostructure Using Reciprocal Lattice Mapping. *Appl. Phys. Lett.* **2012**, *100* (7), 071901.
(9) Annadi, A.; Putra, A.; Liu, Z. Q.; Wang, X.; Gopinadhan, K.; Huang, Z.; Dhar, S.; Venkatesan, T.; Ariando. Electronic Correlation and Strain Effects at the Interfaces between Polar and Nonpolar Complex Oxides. *Phys. Rev. B: Condens. Matter Mater. Phys.* **2012**, *86* (8), 085450.
(10) Pauli, S. A.; Leake, S. J.; Delley, B.; Björck, M.; Schneider, C. W.; Schlepütz, C. M.; Martoccia, D.; Paetel, S.; Mannhart, J.; Willmott, P. R. Evolution of the Interfacial Structure of $LaAlO_3$ on $SrTiO_3$. *Phys. Rev. Lett.* **2011**, *106* (3), 036101.
(11) Maurice, J.-L.; Carrétéro, C.; Casanove, M.-J.; Bouzehouane, K.; Guyard, S.; Larquet, É.; Contour, J.-P. Electronic Conductivity and Structural Distortion at the Interface between Insulators $SrTiO_3$ and $LaAlO_3$. *Phys. Status Solidi A* **2006**, *203* (9), 2209−2214.
(12) Schwingenschlögl, U.; Schuster, C. Interface Relaxation and Electrostatic Charge Depletion in the Oxide Heterostructure $LaAlO_3/SrTiO_3$. *EPL Europhys. Lett.* **2009**, *86* (2), 27005.
(13) Willmott, P. R.; Pauli, S. A.; Herger, R.; Schlepütz, C. M.; Martoccia, D.; Patterson, B. D.; Delley, B.; Clarke, R.; Kumah, D.; Cionca, C.; Yacoby, Y. Structural Basis for the Conducting Interface between $LaAlO_3$ and $SrTiO_3$. *Phys. Rev. Lett.* **2007**, *99* (15), 155502.
(14) Schoofs, F.; Carpenter, M. A.; Vickers, M. E.; Egilmez, M.; Fix, T.; Kleibeuker, J. E.; MacManus-Driscoll, J. L.; Blamire, M. G. Carrier Density Modulation by Structural Distortions at Modified $LaAlO_3/SrTiO_3$ Interfaces. *J. Phys.: Condens. Matter* **2013**, *25* (17), 175005.
(15) Nakagawa, N.; Hwang, H. Y.; Muller, D. A. Why Some Interfaces Cannot Be Sharp. *Nat. Mater.* **2006**, *5* (3), 204−209.
(16) Jia, C. L.; Mi, S. B.; Faley, M.; Poppe, U.; Schubert, J.; Urban, K. Oxygen Octahedron Reconstruction in the $SrTiO_3/LaAlO_3$ Heterointerfaces Investigated Using Aberration-Corrected Ultrahigh-Resolution Transmission Electron Microscopy. *Phys. Rev. B: Condens. Matter Mater. Phys.* **2009**, *79* (8), 081405.
(17) Chambers, S. A.; Engelhard, M. H.; Shutthanandan, V.; Zhu, Z.; Droubay, T. C.; Qiao, L.; Sushko, P. V.; Feng, T.; Lee, H. D.; Gustafsson, T.; Garfunkel, E.; Shah, A. B.; Zuo, J.-M.; Ramasse, Q. M. Instability, Intermixing and Electronic Structure at the Epitaxial $LaAlO_3/SrTiO_3(001)$ Heterojunction. *Surf. Sci. Rep.* **2010**, *65* (10), 317−352.
(18) Salvinelli, G.; Drera, G.; Giampietri, A.; Sangaletti, L. Layer-Resolved Cation Diffusion and Stoichiometry at the $LaAlO_3/SrTiO_3$ Heterointerface Probed by X-Ray Photoemission Experiments and Site Occupancy Modeling. *ACS Appl. Mater. Interfaces* **2015**, *7* (46), 25648−25657.
(19) Kalabukhov, A.; Gunnarsson, R.; Börjesson, J.; Olsson, E.; Claeson, T.; Winkler, D. Effect of Oxygen Vacancies in the $SrTiO_3$ Substrate on the Electrical Properties of the $LaAlO_3/SrTiO_3$ Interface. *Phys. Rev. B: Condens. Matter Mater. Phys.* **2007**, *75* (12), 121404.
(20) Chambers, S. A. Understanding the Mechanism of Conductivity at the $LaAlO_3/SrTiO_3(001)$ Interface. *Surf. Sci.* **2011**, *605* (13−14), 1133−1140.
(21) Liu, Z. Q.; Sun, L.; Huang, Z.; Li, C. J.; Zeng, S. W.; Han, K.; Lü, W. M.; Venkatesan, T.; Ariando. Dominant Role of Oxygen Vacancies in Electrical Properties of Unannealed $LaAlO_3/SrTiO_3$ Interfaces. *J. Appl. Phys.* **2014**, *115* (5), 054303.
(22) Warusawithana, M. P.; Richter, C.; Mundy, J. A.; Roy, P.; Ludwig, J.; Paetel, S.; Heeg, T.; Pawlicki, A. A.; Kourkoutis, L. F.; Zheng, M.; Lee, M.; Mulcahy, B.; Zander, W.; Zhu, Y.; Schubert, J.; Eckstein, J. N.; Muller, D. A.; Hellberg, C. S.; Mannhart, J.; Schlom, D. G. $LaAlO_3$ Stoichiometry Is Key to Electron Liquid Formation at $LaAlO_3/SrTiO_3$ Interfaces. *Nat. Commun.* **2013**, *4* (1), 2351.
(23) Zaid, H.; Berger, M. H.; Jalabert, D.; Walls, M.; Akrobetu, R.; Fongkaew, I.; Lambrecht, W. R. L.; Goble, N. J.; Gao, X. P. A.; Berger, P.; Sehirlioglu, A. Atomic-Resolved Depth Profile of Strain and Cation Intermixing around $LaAlO_3/SrTiO_3$ Interfaces. *Sci. Rep.* **2016**, *6* (1), 28118.
(24) Zaid, H.; Berger, M. H.; Jalabert, D.; Walls, M.; Akrobetu, R.; Goble, N. J.; Gao, X. P. A.; Berger, P.; Fongkaew, I.; Lambrecht, W.; Sehirlioglu, A. Role of the Different Defects, Their Population and Distribution in the $LaAlO_3/SrTiO_3$ Heterostructure's Behavior. *J. Appl. Phys.* **2018**, *123* (15), 155304.
(25) Bark, C. W.; Sharma, P.; Wang, Y.; Baek, S. H.; Lee, S.; Ryu, S.; Folkman, C. M.; Paudel, T. R.; Kumar, A.; Kalinin, S. V.; Sokolov, A.; Tsymbal, E. Y.; Rzchowski, M. S.; Gruverman, A.; Eom, C. B. Switchable Induced Polarization in $LaAlO_3/SrTiO_3$ Heterostructures. *Nano Lett.* **2012**, *12* (4), 1765−1771.
(26) Kumar, A.; Arruda, T. M.; Kim, Y.; Ivanov, I. N.; Jesse, S.; Bark, C. W.; Bristowe, N. C.; Artacho, E.; Littlewood, P. B.; Eom, C.-B.; Kalinin, S. V. Probing Surface and Bulk Electrochemical Processes on the $LaAlO_3$-$SrTiO_3$ Interface. *ACS Nano* **2012**, *6* (5), 3841−3852.
(27) Huang, M.; Bi, F.; Bark, C.-W.; Ryu, S.; Cho, K.-H.; Eom, C.-B.; Levy, J. Non-Local Piezoresponse of $LaAlO_3/SrTiO_3$ Heterostructures. *Appl. Phys. Lett.* **2014**, *104* (16), 161606.
(28) Xie, Y.; Bell, C.; Yajima, T.; Hikita, Y.; Hwang, H. Y. Charge Writing at the $LaAlO_3/SrTiO_3$ Surface. *Nano Lett.* **2010**, *10* (7), 2588−2591.
(29) Li, C.; Cao, Y.; Bai, Y.; Li, A.; Zhang, S.; Wu, D. Electromechanical Response from $LaAlO_3/SrTiO_3$ Heterostructures. *ACS Appl. Mater. Interfaces* **2015**, *7* (19), 10146−10151.
(30) Dai, W.; Adhikari, S.; Garcia-Castro, A. C.; Romero, A. H.; Lee, H.; Lee, J.-W.; Ryu, S.; Eom, C.-B.; Cen, C. Tailoring $LaAlO_3/SrTiO_3$

Interface Metallicity by Oxygen Surface Adsorbates. *Nano Lett.* **2016**, *16* (4), 2739−2743.
(31) Fongkaew, I.; Akrobetu, R.; Sehirlioglu, A.; Voevodin, A.; Limpijumnong, S.; Lambrecht, W. R. L. Core-Level Binding Energy Shifts as a Tool to Study Surface Processes on $LaAlO_3/SrTiO_3$. *J. Electron Spectrosc. Relat. Phenom.* **2017**, *218*, 21−29.
(32) Gariglio, S.; Gabay, M.; Triscone, J.-M. Research Update: Conductivity and beyond at the $LaAlO_3/SrTiO_3$ Interface. *APL Mater.* **2016**, *4* (6), 060701.
(33) Krishnaswamy, K.; Dreyer, C. E.; Janotti, A.; Van de Walle, C. G. First-Principles Study of Surface Charging in $LaAlO_3/SrTiO_3$ Heterostructures. *Phys. Rev. B: Condens. Matter Mater. Phys.* **2015**, *92* (8), 085420.
(34) Pentcheva, R.; Arras, R.; Otte, K.; Ruiz, V. G.; Pickett, W. E. Termination Control of Electronic Phases in Oxide Thin Films and Interfaces: $LaAlO_3/SrTiO_3$ (001). *Philos. Trans. R. Soc., A* **2012**, *370* (1977), 4904−4926.
(35) Scheiderer, P.; Pfaff, F.; Gabel, J.; Kamp, M.; Sing, M.; Claessen, R. Surface-Interface Coupling in an Oxide Heterostructure: Impact of Adsorbates on $LaAlO_3/SrTiO_3$. *Phys. Rev. B: Condens. Matter Mater. Phys.* **2015**, *92* (19), 195422.
(36) Sharma, P.; Ryu, S.; Burton, J. D.; Paudel, T. R.; Bark, C. W.; Huang, Z.; Ariando; Tsymbal, E. Y.; Catalan, G.; Eom, C. B.; Gruverman, A. Mechanical Tuning of $LaAlO_3/SrTiO_3$ Interface Conductivity. *Nano Lett.* **2015**, *15* (5), 3547−3551.
(37) Wang, S.; Bai, Y.; Xie, L.; Li, C.; Key, J. D.; Wu, D.; Wang, P.; Pan, X. Ferroelectric Polarization-Modulated Interfacial Fine Structures Involving Two-Dimensional Electron Gases in Pb(Zr, Ti)O_3 /$LaAlO_3/SrTiO_3$ Heterostructures. *ACS Appl. Mater. Interfaces* **2018**, *10* (1), 1374−1382.
(38) Huijben, M.; Rijnders, G.; Blank, D. H. A.; Bals, S.; Aert, S. V.; Verbeeck, J.; Tendeloo, G. V.; Brinkman, A.; Hilgenkamp, H. Electronically Coupled Complementary Interfaces between Perovskite Band Insulators. *Nat. Mater.* **2006**, *5* (7), 556−560.
(39) Adhikari, S.; Garcia-Castro, A. C.; Romero, A. H.; Lee, H.; Lee, J.-W.; Ryu, S.; Eom, C.-B.; Cen, C. Charge Transfer to $LaAlO_3/SrTiO_3$ Interfaces Controlled by Surface Water Adsorption and Proton Hopping. *Adv. Funct. Mater.* **2016**, *26* (30), 5453−5459.
(40) Li, Y.; Yu, J. Modulation of Electron Carrier Density at the N-Type $LaAlO_3/SrTiO_3$ Interface by Water Adsorption. *J. Phys.: Condens. Matter* **2013**, *25* (26), 265004.
(41) Bi, F.; Bogorin, D. F.; Cen, C.; Bark, C. W.; Park, J.-W.; Eom, C.-B.; Levy, J. Water-Cycle" Mechanism for Writing and Erasing Nanostructures at the $LaAlO_3/SrTiO_3$ Interface. *Appl. Phys. Lett.* **2010**, *97* (17), 173110.
(42) Xie, Y.; Hikita, Y.; Bell, C.; Hwang, H. Y. Control of Electronic Conduction at an Oxide Heterointerface Using Surface Polar Adsorbates. *Nat. Commun.* **2011**, *2* (1), 494.
(43) Collins, L.; Vasudevan, R. K.; Sehirlioglu, A. Visualizing Charge Transport and Nanoscale Electrochemistry by Hyperspectral Kelvin Probe Force Microscopy. *ACS Appl. Mater. Interfaces* **2020**, *12* (29), 33361−33369.
(44) Yu, L.; Zunger, A. A Polarity-Induced Defect Mechanism for Conductivity and Magnetism at Polar-Nonpolar Oxide Interfaces. *Nat. Commun.* **2014**, *5* (1), 5118.
(45) Dai, W.; Yang, M.; Lee, H.; Lee, J.-W.; Eom, C.-B.; Cen, C. Tailoring the Doping Mechanisms at Oxide Interfaces in Nanoscale. *Nano Lett.* **2017**, *17* (9), 5620−5625.
(46) Garrett, J. L.; Munday, J. N. Fast, High-Resolution Surface Potential Measurements in Air with Heterodyne Kelvin Probe Force Microscopy. *Nanotechnology* **2016**, *27* (24), 245705.
(47) Axt, A.; Hermes, I. M.; Bergmann, V. W.; Tausendpfund, N.; Weber, S. A. L. Know Your Full Potential: Quantitative Kelvin Probe Force Microscopy on Nanoscale Electrical Devices. *Beilstein J. Nanotechnol.* **2018**, *9*, 1809−1819.
(48) Nguyen, C. H.; Nigon, R.; Raeder, T. M.; Hanke, U.; Halvorsen, E.; Muralt, P. Probing-Models for Interdigitated Electrode Systems with Ferroelectric Thin Films. *J. Phys. D: Appl. Phys.* **2018**, *51* (17), 175303.
(49) Liscio, A.; Palermo, V.; Samorì, P. Nanoscale Quantitative Measurement of the Potential of Charged Nanostructures by Electrostatic and Kelvin Probe Force Microscopy: Unraveling Electronic Processes in Complex Materials. *Acc. Chem. Res.* **2010**, *43* (4), 541−550.
(50) Kim, Y.; Morozovska, A. N.; Kumar, A.; Jesse, S.; Eliseev, E. A.; Alibart, F.; Strukov, D.; Kalinin, S. V. Ionically-Mediated Electromechanical Hysteresis in Transition Metal Oxides. *ACS Nano* **2012**, *6* (8), 7026−7033.
(51) Balke, N.; Maksymovych, P.; Jesse, S.; Kravchenko, I. I.; Li, Q.; Kalinin, S. V. Exploring Local Electrostatic Effects with Scanning Probe Microscopy: Implications for Piezoresponse Force Microscopy and Triboelectricity. *ACS Nano* **2014**, *8* (10), 10229−10236.
(52) Das, S.; Wang, B.; Cao, Y.; Rae Cho, M.; Jae Shin, Y.; Mo Yang, S.; Wang, L.; Kim, M.; Kalinin, S. V.; Chen, L.-Q.; Noh, T. W. Controlled Manipulation of Oxygen Vacancies Using Nanoscale Flexoelectricity. *Nat. Commun.* **2017**, *8* (1), 615.
(53) Strelcov, E.; Jesse, S.; Huang, Y.-L.; Teng, Y.-C.; Kravchenko, I. I.; Chu, Y.-H.; Kalinin, S. V. Space- and Time-Resolved Mapping of Ionic Dynamic and Electroresistive Phenomena in Lateral Devices. *ACS Nano* **2013**, *7* (8), 6806−6815.
(54) Ding, J.; Strelcov, E.; Kalinin, S. V.; Bassiri-Gharb, N. Electrochemical Reactivity and Proton Transport Mechanisms in Nanostructured Ceria. *Nanotechnology* **2016**, *27* (34), 345401.
(55) Strelcov, E.; Ievlev, A. V.; Jesse, S.; Kravchenko, I. I.; Shur, V. Y.; Kalinin, S. V. Direct Probing of Charge Injection and Polarization-Controlled Ionic Mobility on Ferroelectric LiNbO3 Surfaces. *Adv. Mater.* **2014**, *26* (6), 958−963.
(56) Ding, J.; Strelcov, E.; Kalinin, S. V.; Bassiri-Gharb, N. Spatially Resolved Probing of Electrochemical Reactions via Energy Discovery Platforms. *Nano Lett.* **2015**, *15* (6), 3669−3676.